INTERPRETATION OF RESIDUAL IMAGES: SPECTRAL MIXTURE ANALYSIS OF AVIRIS IMAGES, OWENS VALLEY, CALIFORNIA

GILLESPIE, A. R.[1], SMITH, M. O.[1], ADAMS, J. B.[1], WILLIS, S. C.[1], FISCHER, A. F. III[2], and SABOL, D. E.[1]

[1]. Dept. of Geological Sciences, University of Washington, Seattle, WA 98195, USA.

[2]. Dept. of Natural Resources, Humboldt State University, Arcata, CA 95521, USA.

ABSTRACT

Hyperspectral AVIRIS images may be expressed in terms of mixtures of a small number of spectral endmembers, each of which corresponds to a significant scene constituent. Although the continuum spectra may be well described as mixtures of the spectra of these endmembers, discrete spectral features due to unrecognized or rare scene constituents may not be. In special mixture analysis, the abundances of the endmembers are collected in fraction images. The anomalies are collected in residual images, which are the spectral differences between the modeled and measured data. Root-mean-square residual images, averaged across the spectrum, are sensitive to errors in the continuum model spectrum, but are insensitive to unmodeled narrow absorption features. These are best seen in images of the residuals in each image channel. Detection of unusual scene constituents is enhanced by spectral mixture analysis, but is still limited by sensor sensitivity and the number and width of spectral channels. Mixture analysis has application to remote soil characterization, because of the importance of clay mineralogy, distinguished by weak, narrow absorption bands.

INTRODUCTION

AVIRIS was designed with 224 10-nm channels in order to resolve discrete absorption bands characteristic of many mineral spectra, and to resolve fine structure in vegetation spectra [Goetz *et al.*, 1985]. Much early research with AVIRIS data has focused on this aspect. However, the high dimensionality of the data also offers an unparalleled opportunity to characterize well the continuum spectrum - the major part of the spectrum that lies between small discrete absorption bands. The continuum spectrum offers a store of information about the scene [e.g., Adams *et al.*, 1990b]. Normal concentrations of minerals such as clays or rare earths that may cause local absorption in the spectrum can only be detected and identified against the continuum background, and with a knowledge of what that background signifies in the scene [Shipman and Adams, 1987; Adams *et al.*, 1989; 1990b].

In conventional analyses, the scene is ordinarily taken to consist of pixel-sized elements or tessera of identifiable composition, and a meaningful reflectance spectrum is assumed to exist for each pixel. If the tessera happens to contain multiple components, then it is commonly assumed that a unique mixed spectrum exists for each pixel. If the assumptions are correct, important components may be identified from discrete spectral features in these spectra.

However, a different view of the world is possible, in which a scene is composed of mixtures of a only few components: Aristotle [*ca.* 335 BC], for example, proposed a set of four such endmembers, although not on the basis of their spectral properties. Many natural scenes do appear to be mixtures of a limited number of basic constituents, and the radiant energy from such scenes, measured and displayed as an image, is likewise mixed from energy radiated from these components. It is thus appropriate to analyze images in terms of mixtures; indeed, many images can only be analyzed as mixtures, for the pixel sizes of 5 m or more currently attainable.

In spectral mixture analysis, most of the scene is taken to consist of a few spectrally unique components, the number and identity of which depend upon the spatial scale, spectral resolution, and number of bands of the image [Adams *et al.*, 1989, 1990b; Smith *et al.*, 1990a]. There exists a set of rules governing the spectral mixing of the components. For each pixel, a set of component fractions may be deduced. Each unique pixel spectrum may be estimated from the spectra of the components (endmembers) and their fractions or abundances.

AVIRIS is capable of resolving far more spectral endmembers than is required to reproduce or model the continuum spectrum. If the scene does contain more constituents than is required to reproduce the continuum spectrum, then either these cannot be resolved (ambiguous) or they introduce deviations from the well modeled behavior at only a few wavelengths, as is the case for many minerals with strong absorption bands. These locally absorbing constituents could be regarded as additional endmembers, especially if a second level of analysis was invoked covering only those few bands where they deviated most strongly from the well modeled continuum. However, it is precisely in these absorption regions that linear mixing models function least well [e.g., Shipman and Adams, 1987]. Therefore, we regard the AVIRIS spectrum as consisting of two parts: a well modeled continuum, and a residual spectrum - the observed data minus the estimation [Smith *et al.*, 1988b] - in which information about unusual or unmodeled components may be concentrated. This strategy is best suited for detecting scene constituents having no well-defined absorption features, and low concentrations of scene constituents that do have them. Both these categories of constituents *can only be identified against the continuum background.*

In this paper the general case for linear analysis is investigated. Two AVIRIS images of Owens Valley, California, are analyzed in terms of their spectral mixtures, and the endmember fraction and residual images are constructed. The images were chosen because they depicted previously studied local outcrops of strongly colored epidote-bearing metavolcanic rocks with distinct absorption features, and widespread argillic soils containing small amounts of montmorillonite and kaolinite clays.

Previous Work

The systematics of mixture analysis have been well elaborated in a number of disciplines such as isotopic geochemistry and petrology: for example, Reid *et al.* [1973] used linear mass-balance equations to relate chemical compositions of minerals to chemical composition of lunar samples. The significance of mixtures in multispectral images was recognized at the very beginning of the Landsat era [Horwitz *et al.*, 1971; Detechmendy and Pace, 1972; Hallum, 1972; Nalepka and Hyde, 1972; Sacco, 1972].

Pace and Detechmendy [1973] and Horwitz *et al.* [1975] used linear mixture analysis to estimate proportions of components in mixed pixels, and Richardson *et al.* [1975] developed linear regression models to describe relative amounts of vegetation, soil, and shadow for Landsat MSS data. Ranson [1975] recognized the impact of mixtures on image classification, and Heimes [1977] studied the effects of substrate proportions on spectral reflectance in forests. Kauth and Thomas [1976] considered the changes in spectral mixtures in multitemporal data, and Crist and Cicone [1984] extended this "tasselled cap" analysis to Landsat TM data. Chittmeni [1981] estimated mixture proportions through their region characterization. Adams and Adams [1984] used linear unmixing of MSS images to estimate natural vegetation cover. Much of the agricultural research has been directed towards creating vegetation indexes only, disregarding the compositional differences in the "substrate." However, Huete *et al.* [1985] and Huete [1986] explicitly focused attention on the complex nature of the soil components, and Adams *et al.* [1990a] used spectral mixture analysis of TM images to

differentiate among different types of vegetation in Amazonia. Roberts *et al.* [1990] further explore spectral unmixing to differentiate senescent and woody plant material.

The geologic surface has also received attention. Singer and McCord [1979] proposed unmixing spectroscopic measurements of Mars. Marsh *et al.* [1980] used linear discriminant analysis to estimate constituent proportions in mixed pixels. Dozier [1981] extracted proportions of snow and substrate from multichannel thermal images. Conel and Alley [1984] explored spectral mixture analysis of arid steppe to isolate soil and desert scrub. Smith and Adams [1985a,b] developed an unmixing strategy and applied it to imaging spectrometer data. Pieters *et al.* [1985] showed that spectral mixtures were required to explain lunar images. Adams *et al.* [1986] applied linear mixture analysis to Viking images of Mars. Smith *et al.* [1985] and Mustard and Pieters [1986] estimated abundances from mixed spectra, and Mustard and Pieters [1987] applied these techniques to terrestrial images. Gillespie *et al.* [1986] used linear unmixing of TM images to characterize a desert soil chronosequence. Smith *et al.* [1988a, b] demonstrated that imaging spectrometer calibration could be refined by spectral mixture analysis, requiring only a library of reference spectra. Recently, Boardman [1989] used singular value decomposition and mixing analysis to characterize the spatial scales of spectral variance, and Goetz and Boardman [1989] have suggested spectral unmixing studies as a way to predict the ideal number of channels in hyperspectral images. Gillespie *et al.* [1990] extended spectral mixture analysis to multispectral thermal infrared images.

Spectral data have been treated both as linear and nonlinear mixtures. Linear models are widely, but not universally, applicable to terrestrial satellite images. For example, individual rock types are intimate mixtures of small mineral grains, and their reflectance spectra are nonlinear functions of the spectra of the pure constituents [Adams and McCord, 1972; Nash and Conel, 1974; Johnson *et al.*, 1983, 1990; Pieters *et al.*, 1985; Mustard and Pieters, 1986, 1987; Shipman and Adams, 1987]. Similarly, multiple scattering and transmission in plant canopies produce nonlinear spectral responses [Suits, 1972]. Sasaki *et al.* [1983] used a constrained nonlinear method for estimating endmember proportions. However, intimate mixtures can be treated linearly by converting reflectance to single-scattering albedo [Hapke, 1981; Johnson *et al.*, 1983; 1990]. Additionally, in complex scenes both individual lithologies and plant communities have been regarded as entities having characteristic spectra, which may mix additively with other constituent spectra (references cited above).

During the past decade, we have attempted to formulate a systematic treatment for the general mixing problem - one that is applicable to a wide range of data types and scientific goals [e.g., Adams *et al.*, 1989, 1990b; Possollo *et al.*, 1990; Smith *et al.*, 1990a,b; Gillespie *et al.*, 1990]. Although linear mixing models adequately describe many low-dimensional data such as from Landsat TM, the relation of spectral contrast in absorption bands to abundance of the absorbing material is inherently nonlinear, and more complex modeling is required for many hyperspectral images. To address this issue, Smith *et al.* [1988b] treated AIS (precursor to AVIRIS) hyperspectral data as linear mixtures of endmembers and a residual spectrum, which contained the unmodeled data.

Current Research

In the present paper, we employ a two-stage analysis for AVIRIS images: modeling of the continuum as linear mixtures of the constituents that comprise the bulk of the scene, and isolation of the discrete absorption bands as unmodeled residuals, suitable for later analysis by spectral-matching and band-shape techniques [e.g., Clark *et al.*, 1990]. This analysis differs from previous discussions of spectral mixing by Horwitz *et al.* [1975], Jackson [1983], Conel and Alley [1984], Huete *et*

al. [1985], and Pech *et al.* [1986] in that the approach is directed at using a simple mixture model to link reflectances measured by field and/or laboratory instruments with image relative-radiance measurements acquired by AVIRIS. Although previous studies have discussed the importance of spectral mixtures, they do not provide the methodology to determine the combined atmosphere and instrument calibration at the time of image acquisition, to remove variations in lighting geometry caused by topographic and other factors, and to separate spectral mixtures.

Mathematical Framework

The radiant energy from a scene element, **R**, is integrated over wavelength band **I** and linearly encoded as DN = **g R** + **o** in an image. Parameters **g** and **o** are the calibration coefficients for AVIRIS, and are generally determined by imaging known targets before and during flight [e.g., Chrien *et al.*, 1990; Green *et al.*, 1990]. The measured gray level for each pixel may be described as:

$$DN_i = \sum_{k=1}^{n} f_k \, DN_{ik} + \varepsilon_i \qquad [1a]$$

or, in matrix notation:

$$\vec{D}_m = \vec{f}_n \, [\mathfrak{T}]^T_{m,n} + \vec{\varepsilon}_m \qquad [1b]$$

where **k** denotes each of **n** endmembers comprising the scene, fraction **f** is the abundance of each endmember, **m** is the number of image channels, ε is the remainder between the measured and modeled encoded radiance, $\vec{D}$ is the vector of measured radiances (DN), and $[\mathfrak{T}]$ is the matrix of endmember DN vectors, each referred to as an *image endmember.* The fractional abundances **f** must all sum to unity:

$$\sum_{k=1}^{n} f_k = 1 \qquad [2]$$

The measured spectra may be described as mixtures of **m**+1 endmembers. Generally, fewer endmembers will be used, so that equation 1 is overdetermined. At least one degree of freedom is retained for ε. For low-dimensional systems, **n** may be estimated by the number of eigenvalues for the covariance matrix that exceeds the system noise level.

The radiance from a scene is temporally variable, responding to lighting and viewing geometry and to atmospheric conditions. The radiance also depends upon the scene topography and roughness, as well as the reflectivity. Of the above parameters, only reflectivity is directly related to composition, and as such it is frequently the parameter of greatest interest in interpreting AVIRIS data. For purposes of this discussion, it is assumed that radiance (R_I) and reflectance (r_I) are linearly related as $R_I = a_I r_I + b_I$ [cf. Hapke, 1981; Diner and Martonchik, 1984]. The coefficient a_I includes atmospheric absorption as well as geometric and irradiance terms, and b_I is an atmospheric path radiance term. It is further assumed for simplicity that atmospheric effects are invariant over the scene, although this clearly is an approximation [e.g., Green *et al.*, 1989; Conel *et al.*, 1990; Gao and Goetz, 1990].

Given the above qualifications, the image DN may be related to scene reflectivity and the image endmembers may be expressed as mixtures of more fundamental reflectance spectra:

$$DN_i = (g_i\, a_i)\, r_i + (g_i\, b_i + o_i) \qquad [3a]$$

$$DN_{ik} = g'_i \sum_{j=1}^{n} f_{jk}\, r_{ij} + o'_i + \varepsilon_{ik} \qquad [3b]$$

where $\mathbf{g'_I} = (\mathbf{g_I}\, \mathbf{a_I})$ and $\mathbf{o'_I} = (\mathbf{g_I}\, \mathbf{b_I} + \mathbf{o_I})$; or, in matrix notation:

$$[\mathfrak{I}]_{m,n} = [\sum_{i=1}^{m} g'_i\, \hat{\imath}\,] \left[\, [\mathfrak{R}]_{m,n}\, [f]_{n,n}\, \right] + [\sum_{i=1}^{m} o'_i\, \hat{\imath}\,] + [\varepsilon]_{m,n} \qquad [3c]$$

where $\hat{\imath}$ is the unit vector for the Ith band, and $[\mathfrak{R}]$ is the matrix of **n** reflectance spectra **r**, known as *reference* endmember spectra. Equation 3 relates the image endmembers to global coefficients $\mathbf{g'_I}$ and $\mathbf{o'_I}$, plus $[\mathfrak{R}]$. Using equation 3, $\mathbf{g'_I}$ and $\mathbf{o'_I}$ may be found from the image itself [Smith *et al.*, 1988a,b], with no ground measurements other than those from a generalized spectral library [e.g., Clark *et al.*, 1990]. For real data with measurement errors, equation 3 may not have a unique solution. Gillespie *et al.* [1990] and Smith *et al.* [1990c] describe an indirect method of finding the solution that is most appropriate in terms of the field scientist's observations.

Once the calibrating coefficients and **n** are known, it is possible to describe the image DN for each pixel, not just the image endmembers, in terms of mixtures of the chosen set of reference endmember spectra:

$$DN_i = g'_i \sum_{j=1}^{n} f_j\, r_{ij} + o'_i + \varepsilon_i \qquad [4a]$$

or, in matrix notation:

$$\vec{\mathfrak{D}}_m = \vec{g'}_m \left[\, \vec{f}_n\, [\mathfrak{R}]^T_{m,n}\, \right] + \vec{o'}_m + \vec{\varepsilon}_m \qquad [4b]$$

The goal of subsequent analysis is to find the endmember fractions $\mathbf{f_j}$ for each pixel of the image. It should be clear from equation 3 that this is possible by inversion. For example, given the case with two image channels and three endmembers,

$$\begin{aligned} f_1 &= \{ (D_1 - r_{13})\,(r_{22} - e_{23}) - (D_2 - r_{23})\,(r_{12} - r_{13}) \} \div \\ &\quad \{ (r_{11} - r_{13})\,(r_{22} - r_{23}) - (r_{21} - r_{23})\,(r_{12} - r_{13}) \} \\ f_2 &= \{ (D_2 - r_{23}) - f_1\,(r_{21} - r_{23}) \} \div \{ r_{22} - r_{23} \} \qquad [5] \\ f_3 &= 1 - (f_1 + f_2) \end{aligned}$$

where $D_l = (DN_l - o'_l) / g'_l$ and, because this particular solution is exactly determined, $\varepsilon_l = 0$. The explicit expression for the endmember fractions is more complicated for more channels and endmembers than used for equation 5. In general, equation 4 will be overdetermined, and may be solved by least-squares methods.

The products of spectral mixture analysis are thus sets of **n** reference spectra and fraction images depicting their abundances in the scene, and **m** residual images containing the difference between the modeled and measured data.

METHODOLOGY

Image Endmembers

The first step in analyzing the AVIRIS images is to determine the number and identity of the image endmembers that are necessary to model the continuum spectrum. The image endmembers - the DN vectors on the right-hand side of equation 1 - are generally extracted from the image itself, not from a reference spectral library, and as such they typically do not represent "pure" scene constituents, but are themselves mixed from more basic reference spectra.

The number of endmembers is one more than the number of dimensions required to explain the data variance, or the number of channels actually required to describe the spectral constituents of the scene. This number, the *intrinsic dimensionality* of the data [Possollo *et al.*, 1990], may vary from image to image. Spectral data are typically redundant [e.g., Adams *et al.*, 1989; 1990b] and the intrinsic dimensionality may be much smaller than the number of channels of data acquired by AVIRIS.

The intrinsic dimensionality is determined from analysis of the image, where possible after nominal calibration to radiance using preflight data [e.g., Otterman *et al.*, 1980; Chrien *et al.*, 1990] and atmospheric corrections [e.g., van den Bosch and Alley, 1990]. For low-dimensional data, it is approximated by the number of eigenvalues of the covariance matrix that exceeds the noise variance of the system. This estimate is refined by inspection of data spaces in which selected transects from the image are displayed [e.g., Buja and Asimov, 1985]. For AVIRIS data, inverting the entire covariance matrix to find the eigenvalues is impractical, and we make an initial estimate from the number of eigenvalues for a subset of grouped channels, which together span the AVIRIS spectrum. In this way, the dimensionality of the continuum spectrum - but not of the entire spectrum containing sharp absorption features - is approximated. Scene constituents spectrally distinguished only by local departures from the continuum (low concentrations, sharp absorption features) are not treated as endmembers, but are concentrated in a residual spectrum, discussed below.

Principal-component analysis permits approximation of the intrinsic dimensionality, but it provides little information on which endmembers are important and with which other endmembers they mix. Inspection of data clusters is necessary to determine which endmembers mix together, to identify "extreme" pixels that consist dominantly of a single endmember, and to identify which endmembers comprise the bulk of the data. During inspection of the data clusters, the binary mixing lines connecting the tangible endmembers with shade also are identified, and their intersection is found in order to estimate the shade endmember, as discussed below. In contrast to the principal axes, the endmember vectors generally are not orthogonal in the original data space. Sabol *et al.* [1990] discuss the consequences of nonorthogonality on fraction resolution and endmember detectability.

Once a list of candidate image endmembers has been made, a final estimate of **n** is made by tentative solutions of equation 1 using successively greater values of **n** until the root-mean-square (rms) residual $((\mathbf{m}^{-1}\Sigma(\varepsilon_i^2))^{1/2})$ is reduced to the noise level (i.e., 1-2 DN). The first iteration uses only the two or three best-defined image endmembers. The rms residual image is inspected to determine how well the image is fit by the selected endmembers and, equally important, where the fit is worst. DN vectors from the worst-fit areas are compared to the list of unused image endmembers, and - one by one - new endmembers are used in solving equation 1 until the entire rms image (or at least the part of interest to the analyst) has a DN level comparable to image noise. From our experience, this will generally be at a level of DN < 2 for AVIRIS. Equally important, when the image is properly modeled it will generally not be possible to see much structure other than microphonic noise in the rms residual image.

In the above strategy, the image endmembers are selected by meeting the formal requirements sequentially, not in one step. This approach conforms with that of both Possolo *et al.* [1990] and Huete [1986].

Finding Shade

Topographic shadows and photometric shading differ from the atmospheric and global irradiance terms that influence measured radiance in that they are spatially variable at the pixel scale. Thus they cannot be described by the coefficients $\mathbf{g'}_i$ and $\mathbf{o'}_i$. In a calibrated image, topographic shadows and photometric shading together act as a zero-reflectance endmember that we refer to as "shade" [Adams et al., 1986; Smith et al., 1990a]. From a single AVIRIS image, it is difficult to distinguish the darkening due to photographic (Lambertian) shading from darkening caused by discrete subpixel shadows. The shade endmember is spatially and temporally variable and contrasts conceptually with the other, "tangible" endmembers that correspond to physical scene constituents that change slowly if at all.

In a single image of a scene it may not be possible to distinguish shade from darkening due to low albedo. Resolution of inherently dark surfaces is possible using multitemporal data, which is beyond the scope of the present discussion.

A satisfactory image endmember for shade [Richardson *et al.*, 1975; Adams *et al.*, 1986; Ranson and Daugherty, 1987; Smith *et al.*, 1990a; Roberts *et al.*, 1990] requires that multipixel shadows on a black surface exist somewhere in the image. Although in the first stages of analysis the "darkest pixel" is sometimes used as the shade vector, the darkest pixel generally contains contributions from illuminated as well as from shaded or shadowed scene constituents, and in any case the reflectance is greater than zero. Consequently, for refined analysis, in most images the shade image endmember must be estimated from the distribution of the image data in the DN space.

The strategy is to find a group of pixels comprising only one or two tangible endmembers, but a range of illumination geometries. In DN space, these data will be distributed along one or two binary mixing lines connecting the lightest and darkest scene elements. If different mixing lines are present, they will converge towards a common small (dark) DN vector, although the intersection will not itself be observed. The locus may be found graphically, a tedious procedure for AVIRIS data, or it may be estimated from the closest approach of lines regressed to two or more binary mixing clusters. In general, shade will lie close to the principal axis of the data, so that it may be approximated well even if the DN value for only a single channel is found by triangulation. In finding shade, it is important to note that shadows cast by leafy vegetation contain green and near-infrared light transmitted through the leaves, and are not described by the same vector as shadows from opaque objects [Roberts *et al.*, 1990].

Reference Endmembers

Transforming the AVIRIS image to fractions of image endmembers is useful, but does not realize the full power of spectral mixture analysis. This is because the image endmembers themselves may be mixtures of still more basic or spectrally extreme scene constituents. The image endmembers are derived from the image itself, and if no "pure" pixels are encountered, the endmembers will be impure also.

The next step in analysis is to select a subset of spectra from a reference library that, in the experience of the analyst, is likely to be encountered as scene constituents. The choice of individual spectra is not too important, provided a sufficiently wide range is represented. It is better to include too many than too few reference spectra. In our experience with Landsat TM, the preliminary list of reference endmembers may include 60 - 100 spectra. Because AVIRIS spectra have more detail, more reference spectra may be useful. However, this is not a foregone conclusion: because of the way in which we divide the spectrum into a continuum and residual part, the number of endmembers is not necessarily related to the number of image channels, and the number actually chosen is likely to be on the order of ten.

After selecting a pertinent subset of the reference library, the reference spectra are grouped by scene constituent: e.g., riparian vegetation, carbonate rocks, and so forth. These groups include those needed to describe the image endmembers. The library is sampled again, this time into a large number of subsets of **n** spectra each, where **n** is the number of image endmembers. Each spectrum in each sample is drawn from a different group; the same groups may be represented in each sample.

The **n** image endmembers (DN) are modeled as mixtures of the **n** reference spectra (reflectance) in each sample, first using a method of successive approximation to solve equation 3 for the calibration coefficients, **g'** and **o'** [e.g., Gillespie *et al.*, 1990]. Because of system noise, direct inversion of equation 3 to solve for the calibration coefficients and endmember fractions simultaneously may not be feasible: there may be multiple apparent solutions. The first approximation is to assume values for the reference endmember fractions $\mathbf{f}_j$, based on any available information, including ground measurements and observations, photointerpretation and past experience. For reasonable subsets of reflectance spectra, the calibration coefficients will cluster about central values. Because the AVIRIS data have already been nominally calibrated, the remaining calibration basically corrects for atmospheric effects, plus minor changes in AVIRIS sensitivity during flight. Thus the values of the calibration coefficients determined above may be predicted fairly closely. Subsets requiring greatly different coefficients are rejected, and the list of candidates is narrowed.

The second approximation is to assume the value of the calibration coefficients, generally the mode or mean of the found values. Equation 3 is solved again for the remaining subsets of reference spectra. This time **f** values are tabulated, and the list of spectra is winnowed further.

The next steps involve successively closer approximation to the "correct" values of **g'**, **o'** and **f**, and further winnowing. At this level of analysis, it is likely that many values for the calibration coefficients and endmember fractions will cluster tightly, such that it is not obvious which reference spectra fit the image endmembers best. New criteria are invoked to proceed with the winnowing process: the sets that are retained are the ones for which the rms residuals are smallest. Ultimately, it is possible to narrow the choice to at most three or four sets of similar spectra.

It is next useful to solve equation 4 for fractions and residuals for the remaining sets of reference spectra. This step differs from the previous ones in that it is the image, not the set of image endmembers, that is recast in terms of the reference spectra. Final refinement of the calibration coefficients and the choice of endmembers is made in light of spatial patterns in the residual and fraction images. This is a

powerful advantage that may not be evident at first glance, because it brings into play the considerable range of skills and experience of the photointerpreter and field scientist. This step in the analysis involves inspecting fraction images for large out-of-bounds areas ($0 \leq f_k \leq 1$). Strictly, subzero or superunitary fractions mean only that the endmembers have less spectral contrast than the data; mathematically, the solution may be satisfactory. Nevertheless, it may be desirable to choose more extreme spectra from the same groups.

An rms residual image calculated for the chosen reference endmembers is inspected for areas of high DN and spatial structure pertinent to the scene rather than to image noise. The fraction images themselves are then studied for conformity to what is known about the scene: i.e., areas of known vegetation should have high f-values in the vegetation image. Finally, band-residual images (ρ_I) are constructed for each channel, and studied for areas that are not well modeled. It may be necessary to return to solving equation 3 in light of the experience gained with the image data; but, if this is the case, it will be with a much narrower range of reference spectra and a refined concept of the range of valid calibration coefficients and endmember fractions.

Many of the ambiguities in choosing reference spectra arise because there is little difference between the candidates: either would suffice as an endmember. It is necessary to recall that for the fractions to have quantitative significance in terms of scene constituents, they must be calibrated to field measurements [e.g., Smith *et al.*, 1990a]. If the "wrong" endmember is selected, in general the main effect will be an adjustment of the calibration relating the endmember fractions to field measurements of scene constituents. The fit of the model to the data may also be affected, and in this case there may be a change in the rms residual image. Finally, if one of the ambiguous endmembers has more local spectral contrast or structure than the other, the individual band-residual images may differ. It is important to emphasize this trade-off, because it may happen that there is no obviously "correct" endmember.

Band Residuals

Band residual images are calculated by subtracting the continuum model from the observed data, band by band. They differ from the rms residual image, which is averaged across the spectrum. Positive anomalies occur when an absorption feature in the endmembers is not found in the data; negative anomalies occur when the data contain such a band, but not the endmembers.

The continuum model is based on a small number of endmembers, and spectral information describing all the other scene constituents resolvable by AVIRIS will be concentrated in the residual spectra. The information contained in the residual spectrum may be studied by further mixture analysis, or by other approaches that focus on specific band locations and depths [e.g., Clark *et al.*, 1990]. Band residual images differ from the rms residual image in that the rms data describe the fit of the model in a general sense, over the entire spectrum, whereas the band residual data refer to a single wavelength or image channel only.

It is advantageous before analysis of specific absorption features to remove the continuum spectra defined by the handful of endmembers that together comprise most of the spectral variance of the scene. In part this is because the interference of different features is reduced. For example, the spectrum of vegetation is convex near the 2.2-μm absorption bands in clays [e.g., Roberts *et al.*, 1990]; inspection of the mixed spectrum from vegetation and clays might lead to a bad estimate of the band depth, or in noisy data the clay bands might be obscured entirely. The amount of vegetation present is estimated from the entire spectrum, however, not just from a small suspect window, and the vegetation fraction may be determined precisely. Thus the correction of the spectrum near 2.2 μm for vegetation is also precise, and the residual spectrum contains only information from the clay-rich substrate.

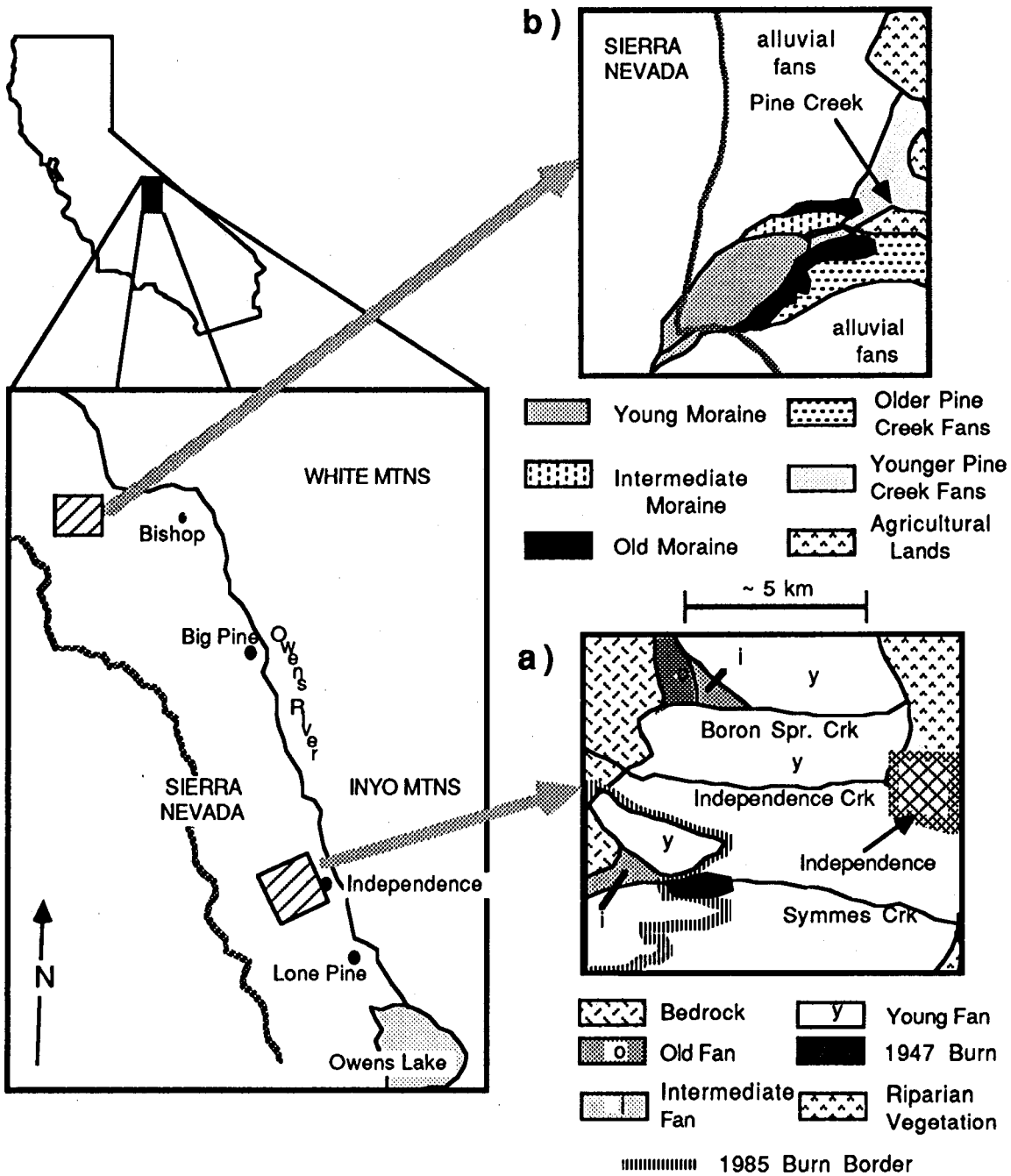

Figure 1. Index and interpretive maps of California showing AVIRIS study areas in Owens Valley. **a)** Independence Creek. **b)** Pine Creek.

Band residual data are displayed to good advantage in image format. This is because localized concentrations of unusual, unmodeled endmembers stand out well when the images are scanned sequentially, in order of wavelength. Where the measured spectrum is well modeled, scene detail will be lacking in residual images, but at

wavelengths where the fit is not as good, structural information will be evident. Once an anomalous area is identified in the residual images, it is possible to display the data for that region as a spectrum, devoid of spatial context, for conventional analysis [e.g., Goetz *et al.*, 1982; Vane and Goetz, 1988].

APPLICATION

We applied spectral mixture analysis to two AVIRIS images of different scenes in Owens Valley, California: Independence Creek, west of the town of Independence, and Pine Creek, northwest of the town of Bishop (Fig. 1). Both were acquired at ~18:15 GMT, shortly before local noon, 14 June 1989. Both scenes contained examples of minerals - especially epidote and clays - with strong absorption bands, present in minor amounts. These minerals might be expected to affect residual images, but not endmember fraction images. We expect the minerals sought for in this example to be difficult to identify in conventional approaches, because they are present only in low concentrations.

Desert scrub of the Great Basin sage community (*Artemisia*, *Coleogyne*, *Purshia*, *Ephedra*) covered both study areas ~20-50%. The alluvial fans of the Independence area were previously modeled using the six-channel Landsat TM data and a four-endmember model [Smith *et al.*, 1990a]. Certain critical scene constituents were ambiguous to TM: for example, argillic soils could be modeled as mixtures of vegetation, and different ferrihydrite-rich soils, and wood, bark and vegetation litter masqueraded as weakly developed soil. AVIRIS offers the possibility of making these and other important distinctions directly. However, our results will show that AVIRIS required no more endmembers than TM to model the continuum spectra accurately. The remaining information lies in the residual data. Figure 1 provides geologic sketches of the two study areas, discussed in their respective sections below.

The AVIRIS data, before spectral resampling, were analyzed using WISP, an interactive image analysis system developed and implemented in LISP on Symbolics computers at the University of Washington [Shippert *et al.*, 1988]. A Pixar is peripheral to one of the Symbolics, and permits the rapid processing of large amounts of data. The Pixar was used to scroll through a spatial subset of the AVIRIS images, channel by channel, to select the bands for spectral mixture analysis. Images channels were rejected if they were obviously noisy or if they were in atmospheric water-absorption bands (~1.4 and 1.9 μm). Very few channels outside of the water bands were unuseable, and 171 channels were accepted. Using the Pixar, data from all these channels were unmixed simultaneously, rather than hierarchically, in different steps for each spectrometer or spectral region within the AVIRIS window. Reference endmembers were chosen from a preliminary list of 96 reflectance spectra.

Spectra of Epidote and Clay-Bearing Soils

Figure 2 shows that reflectance spectra for both epidote and a sieved sample (~100-μm grain size) from the surface of a desert soil have similar overall convex shapes in the spectral region 0.4 - 2.5 μm. In each case, the rising slope of the spectrum at wavelengths <1 μm is due to absorption by Fe^{3+}, and the falling slope beyond 2 μm is due to OH^-. The overall reflectance is also influenced by particle size.

Ionic absorptions are also responsible for deviations from the continuum spectra. A broad, weak Fe^{++} is seen in the soil spectrum near 1 μm (arrow), and a narrower feature near 2.2 μm (arrow) is attributed to OH^- in clay. There is a hint of a $CO_3^=$ band near 2.3 μm. The Fe^{++} is probably due to unweathered mafic minerals, and will only weaken with further soil development. The OH^- is attributable to clay

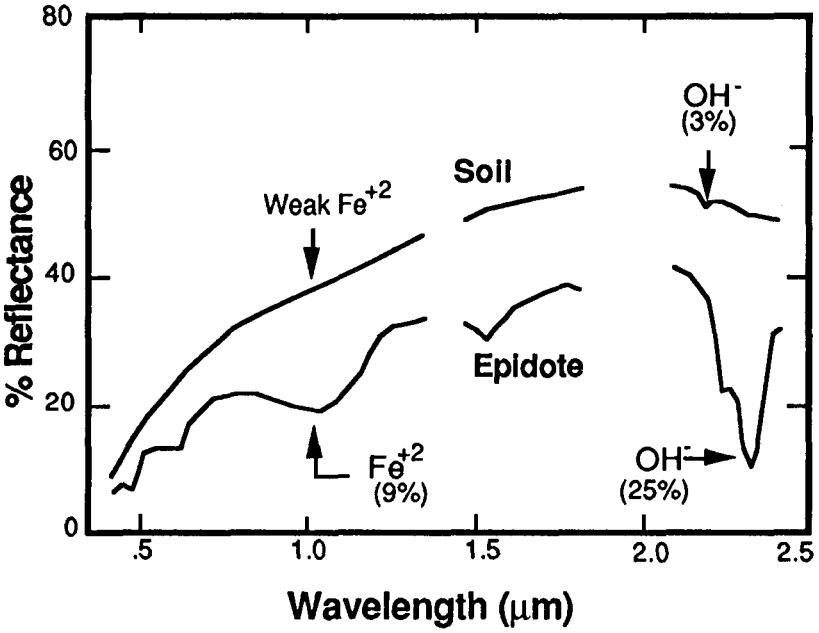

Figure 2. Laboratory reflectance spectra for a clay-bearing soil and for epidote in metavolcanic rocks, Independence Creek. The spectra have been convolved with the 171 AVIRIS bands used in the mixture analysis; gaps near 1.4 and 1.9 μm are the locations of major atmospheric water absorption bands. Selected absorption features and band depths are indicated.

coatings on sand grains [Burke *et al.*, 1986]. Although the soil is well developed for eastern California, the spectral contrast is only 0.03 reflectance units. This band depth is close to the resolution limit of AVIRIS spectrometer D (~0.02).

The epidote spectrum shows several deep discrete bands due to Fe^{3+} and Fe^{++} at wavelengths < 1.4 μm. However, the most prominent feature, near 2.3 μm, is due to OH^- and has a depth of 0.25 reflectance units.

The epidote spectrum shows stronger discrete absorption features than the soil spectrum, at least at the scale of the laboratory spectrometer measurement (2 cm). However, at the scale of AVIRIS measurement (~10 m) epidote is present in much lower concentrations, and the spectral features will be proportionately weaker, whereas the soil spectrum is representative of even larger areas.

The major absorptions that determine the overall shape of the spectra will be described by mixtures of endmembers during mixture analysis. The goal of the present investigation is to recognize the discrete absorption features in the band-residual images over soils of Owens Valley and epidote-bearing rocks along Independence Creek.

Independence Creek

The Independence Creek study area was chosen because it encompassed both an outcrop of metavolcanic rocks containing epidote, and a soil chronosequence developed on granitic alluvial fans containing montmorillonite and kaolinite clays. Figure 1 gives a geologic interpretation of the study area. Most of it falls on the bajada, here consisting of the alluvial fans of Independence Creek and adjacent drainages. The image spans the fans, from their heads on the Sierra Nevada range front to their toes in the fluvial sediments of Owens River. The fans are of different ages, ranging from ~10^4 to $5x10^5$ years. Because deposition was episodic, corresponding to major glaciations, there are large areas of uniform soil development, proportional to age. The soils are non-calcic, and the chief weathering products are ferrihydrite and montmorillonite clays on the younger fans, with the addition of kaolinite on better developed soils. Discrete areas of different development are seen on the fans north of Independence Creek, near the Sierra Nevada range front.

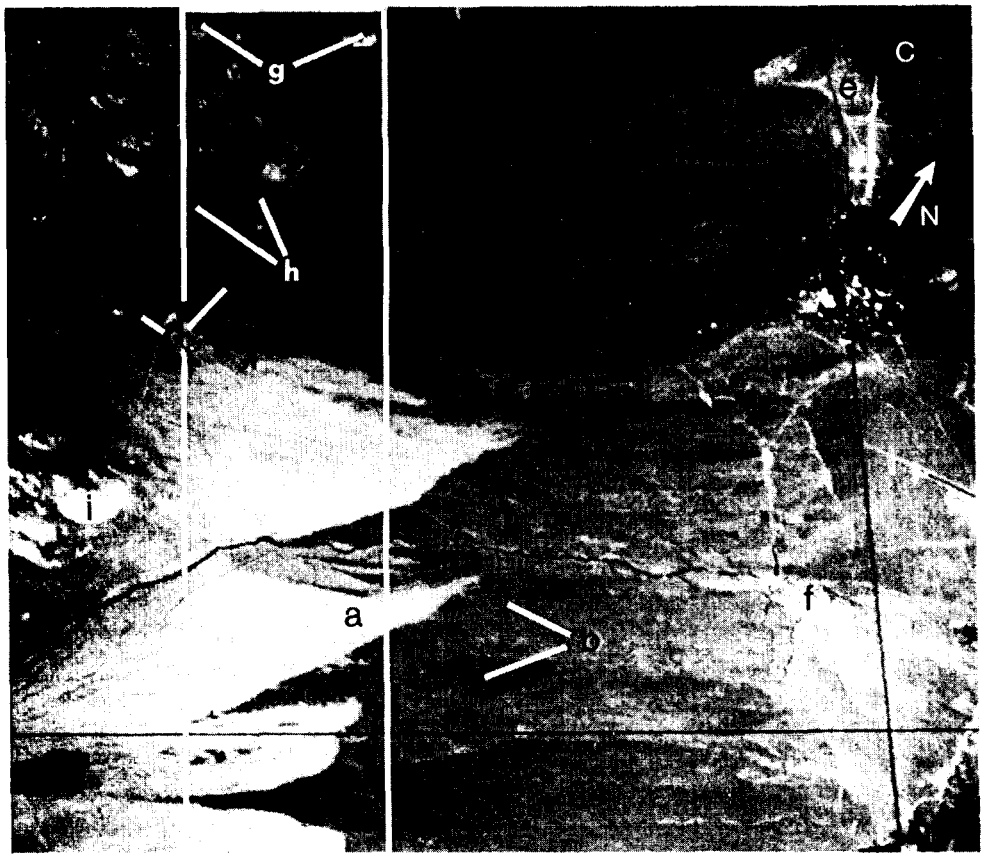

Figure 3. Single band (0.554 μm) of the AVIRIS image of Independence Creek. Scene is approximately 9 km across. Image strip for which band residuals were calculated is outlined. Letters *a* - *i* denote areas discussed in the text.

The fans are covered uniformly with 30-50% desert scrub [Smith *et al.*, 1990a]. Along Independence Creek and on the valley floor are more densely vegetated areas, generally dominated by oak and cottonwood trees, or agricultural fields. Along the contact between fans and fluvial sediments is a zone of dry grasses and brush, including Russian thistle.

The fans and valley floor are subject to range fires, and a major recent (1985) fire at Symmes Creek has denuded the upper reaches of the alluvial fans south of Independence Creek (Fig. 1). At the time of AVIRIS image acquisition (1989), only a fraction of the bushes had recovered, but dry annuals and grasses were common. Along Symmes Creek itself, a smaller older (1947) burn scar is also visible. The fires covered areas of different degrees of soil development: west of the 1947 scar, visibly reddish soils (~ 150 ka) are exposed in contact with a range of less-developed soils to the north. The strong winds that accompany the fires can mobilize the upper few cm of the soils, moving silt and clays great distances and creating low-amplitude dunes of sand and pea-gravel [Bierman and Gillespie, 1990]. The burn scars are interesting in terms of spectral mixing because they provide views of the same soils with different patterns and density of vegetation.

The bedrock lithologies of the Sierra Nevada range front are dominantly granitic, with scattered metamorphic pendants. The granitic rocks spall during range fires and shed grus as they weather, providing an unstable surface for the growth of

lichens and coating by desert varnish. Exposed metavolcanic rocks do not become grusy, but they do spall and shatter. Epidote is a widespread alteration product in the metavolcanic rocks and, disseminated in microcrystalline form, it is probably ubiquitous. Local concentrations also occur, in which some coarser epidote crystals up to 1 mm in diameter are also found. Some of these concentrations are in cm-thick veins, but others are in patches or vein aggregates ranging upwards in diameter to ~100 m. Nevertheless, abundance rarely exceeds a few percent.

The AVIRIS image of Independence Creek (Fig. 3) shows the bajada as uniformly gray, with subtle tone differences due to variation in lithology and, especially, in vegetation density. The fire scars are the most prominent aspect of the image (a). Soil development differences on the bajada are subtle (b). Riparian vegetation on the valley floor and along the streams is dark (c,d), but the dry vegetation at the toes of the fans does not stand out (e). Light-colored patches there are sandy areas, in part along aquifer recharge canals south of Independence Creek (f). Granitic bedrock (g) is light, whereas the metavolcanic outcrops (h) are very dark. Where granitic bedrock is exposed in the fire scars (i) it is even lighter. This is a measure of the extent of darkening of the unburned surface due to vegetation and rock varnish.

The AVIRIS data for the bajada were found to have an intrinsic dimensionality of only three. Smith *et al.* [1990c] give an extended discussion of the choice of endmembers and the range of candidates. Four reference endmembers corresponding to moderately developed reddish and weakly developed sandy soils on granitic alluvium, desert scrub vegetation (*Coleogyne*) and shade were selected. Riparian vegetation and dry grass were equally valid candidates, but were not present in large amounts on the bajada and were not used.

Fraction images for two of the reference endmembers are presented in Fig. 4. Figure 4a shows the fractions for the moderately developed reddish soil. The chief patterns in the image are the low fractions over the recent fire scar (a), especially over the less developed soils on the younger fans (b). Along Symmes Creek near the range front, old fans within the scar (c) have the same fractions as across the boundary (d). The rest of the bajada (e) appears as mottled gray, with patterns delineating fan units according to age, as verified in the field. In general, bedrock outcrops have high fractions, and so do some - but not all - heavily vegetated areas. This phenomenon is best observed along Independence Creek (f) and at the distal ends of the fans (g). Lastly, a zone extending beyond the perimeter of the recent fire scar is locally light in the fraction image, always on the southeast side of the scar (h).

Figure 4b shows the fractions for the sandy soil. It is in many respects the complement of Fig. 4a. However, over all heavily vegetated areas (i,j) the soil fractions are both low. Were there additional soil endmembers, the complementary fractions would be less common.

The four continuum reference endmembers together accounted for all except 1-4 DN of rms residual data, over all bands (Fig. 5). Over most of the bajada and foothills of the Sierra Nevada, the rms residual was about 1 DN. This low value is close to the noise level of AVIRIS; nevertheless, the rms image does show scene detail that would not be evident in a TM residual image at 1 DN. This increased resolution we attribute to the large number of bands in AVIRIS.

The greatest rms residuals occurred in the riparian vegetation (a), metavolcanic rocks (b), and south-facing slopes of granitic bedrock in the burned areas (c). The riparian vegetation and the metavolcanic rocks were not represented by an endmember in the analysis, but the granitic rocks were spectrally similar to the sandy soil endmember. The metavolcanic rocks were of low albedo, and were not assigned an additional endmember because it would be so similar to shade that the two fraction images would appear "noisy."

Figure 6 shows band residuals for three selected spectral windows predicted from the spectra of epidote and/or soils (Fig. 2) to have absorption features. Every

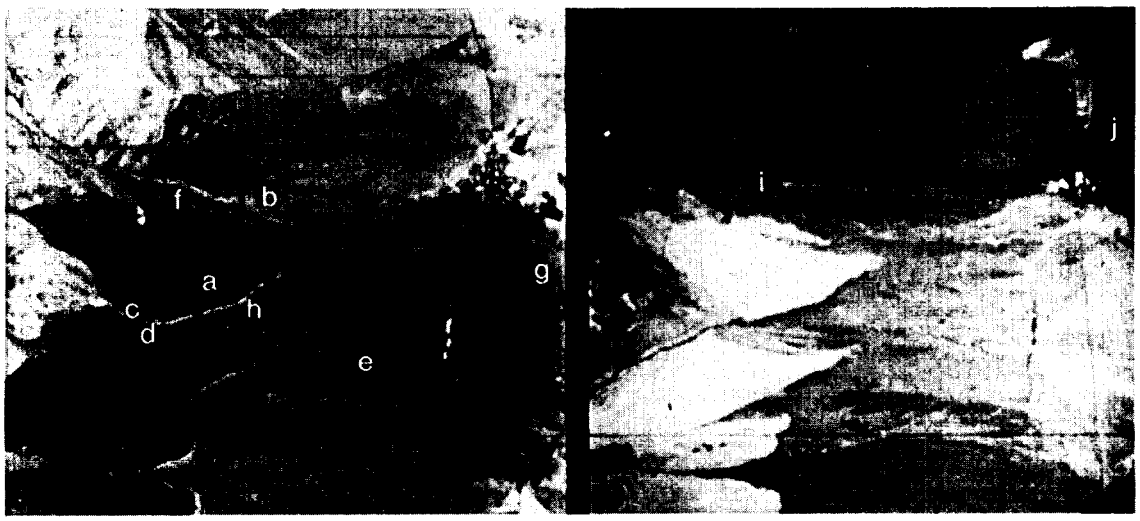

Figure 4. Two reference endmember fraction images, Independence Creek (light = high; dark = low). **a)** Well developed oxidized and argillic granitic soil. **b)** Weakly developed sandy granitic soil. Letters *a* - *g* denote areas discussed in the text.

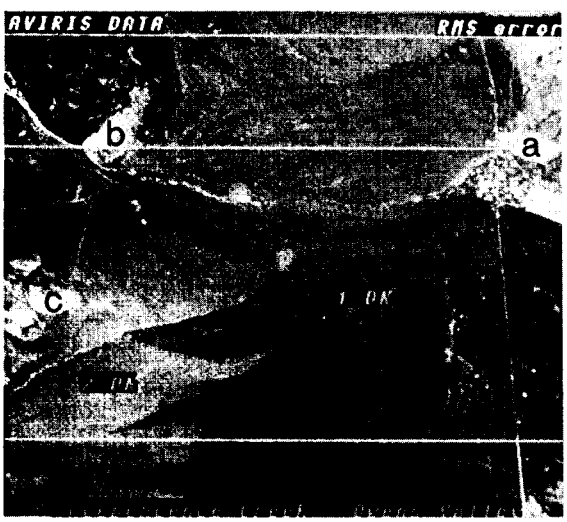

Figure 5. RMS residual image of Independence Creek. The image has been strongly stretched to reveal detail. The original data range was 0 - 4 DN. Lettered features are explained in the text.

third 10-nm band within each window is displayed, although all were calculated and inspected. The residuals were uniformly contrast-stretched for display such that the total range was ±3 DN, with negative values dark and positive values light. The residuals were calculated for the vertical image strip outlined in Fig. 3.

Figure 6a shows the residual data for a 21-band span in the visible spectrum. These residual images superficially resemble the radiance data (e.g., Fig. 3), but upon close inspection differences are evident. The positive spectral contrast between the burned (a) and unburned sandy alluvium (dark) peaks at 0.554 μm; the unmodeled residual in either case is quite small at shorter wavelengths, and the contrast lessens at longer wavelengths. This lessening of contrast is not as pronounced for the older alluvium in the fire scar (b). The unburned fan at (c) shows an interesting reversal

of contrast between residuals for the reddish and sandy soils. At wavelengths ≤0.554 μm, the reddish soil appears neutral, whereas the sandy soil appears light. At 0.613 μm the residuals are both moderately high, and above 0.643 μm the reddish soil is the lighter. The quartz monzonite bedrock (d) has a residual peak near 0.584 μm, and an epidote-rich zone (e) within the metavolcanics has a residual minimum centered near 0.6 μm. The peak for the quartz monzonite is most prominent on south-facing slopes, and it is therefore tempting to attribute it to an error in the shade vector, but were this the case the sunlit/shaded contrast would persist across a wide range of wavelengths, and it does not.

Figure 6b shows the residual strips from 0.931 to 1.183 μm, spanning the minimum of a major Fe^{++} absorption in epidote. The residual images have enhanced contrast from 0.989 to 1.076 μm, with the sense of the residuals similar to Fig. 6a, for many of the same features. The burned areas and granitic bedrock are light, and the metavolcanics are dark. The sunlit/shaded slopes appear anomalous in the same way as before. However, the fans at (c) are not associated with any positive or negative residuals, and the contact cannot be detected in Fig. 6b. The southeastern margin of the 1985 fire scar just north of Symmes Creek (f), appearing to have a high fraction of reddish soil in Fig. 4, shows a higher positive anomaly than the scar itself from 1.076 to 1.134 μm. Lastly, trees bordering Independence Creek (g) have a positive anomaly from 1.076 to 1.185 μm.

Figure 6c shows residuals in the 2.2-μm region, where both clays and epidote have absorption bands. Excess montmorillonite that is not accounted for by the reddish soil endmember should show as a narrow negative anomaly centered at 2.2 μm; epidote should show a wider negative anomaly deepening with wavelength, because the center of the absorption band is > 2.252 μm (Fig. 2). However, these patterns are not observed, and across the entire window the continuum model appears to fit the data well, within the noise limits imposed by spectrometer D (~0.02 reflectance units).

Figure 6 is effective in showing spatial characteristics of relative anomalies in band-residual data, but less well suited for showing the shape or actual magnitude of

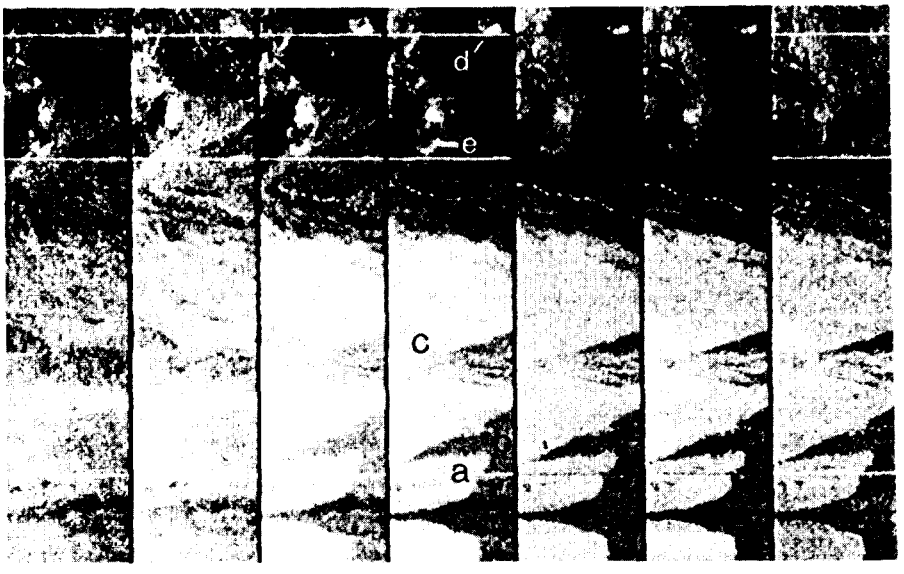

Figure 6. Band-residual image strips, for three spectral regions. The strips are from the image area outlined in Figure 3. Letters denote areas explained in text. a) Visible (0.49 - 0.67 μm). b) Near - infrared (0.93 - 1.16 μm). c) Near - infrared (2.19 - 2.25 μm).

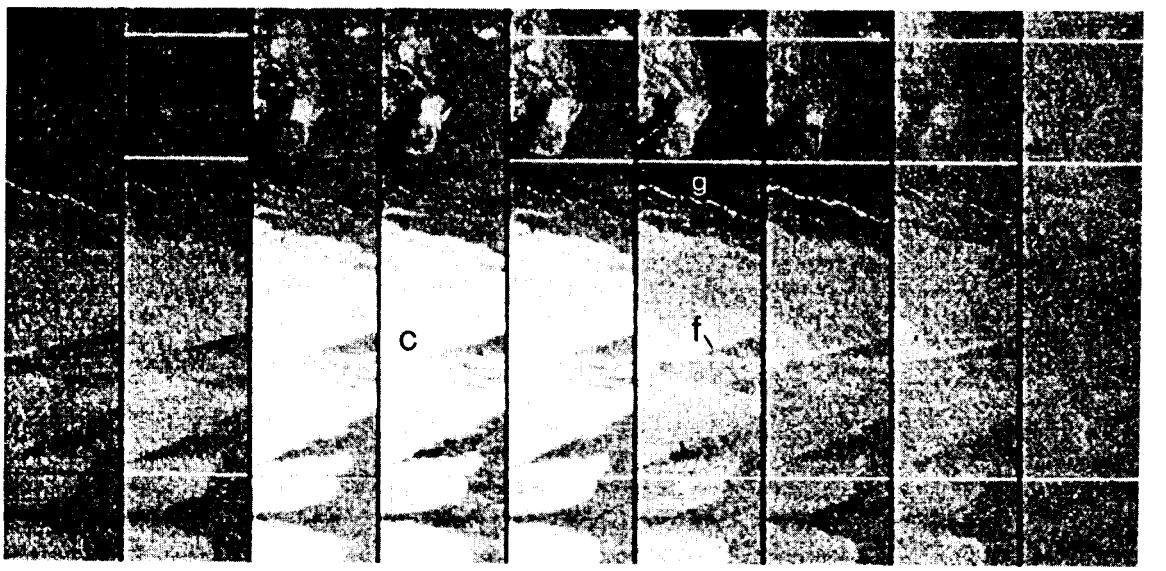

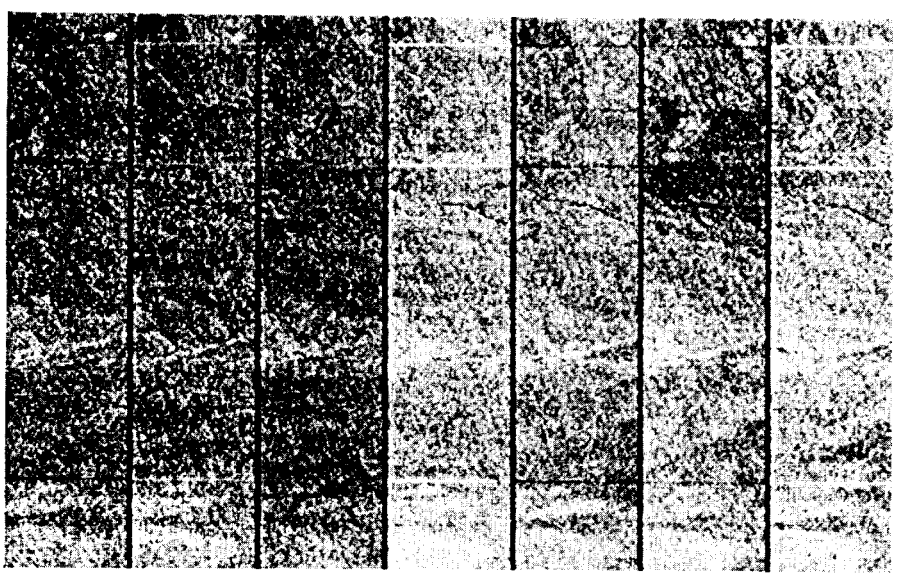

(Figure 6b, c, Band - residual images.)

the anomalies. In Figure 7, spectra from two of the anomalous areas from Fig. 6 are graphed, for the middle spectral window (~1 μm). Feature A has a broad positive anomaly, roughly 0.03 reflectance units in height. It is associated with the quartz monzonite bedrock, the spectrum being taken from an outcrop at the northern end of the same meta-andesite ridge that had the highest concentrations of epidote. Residual

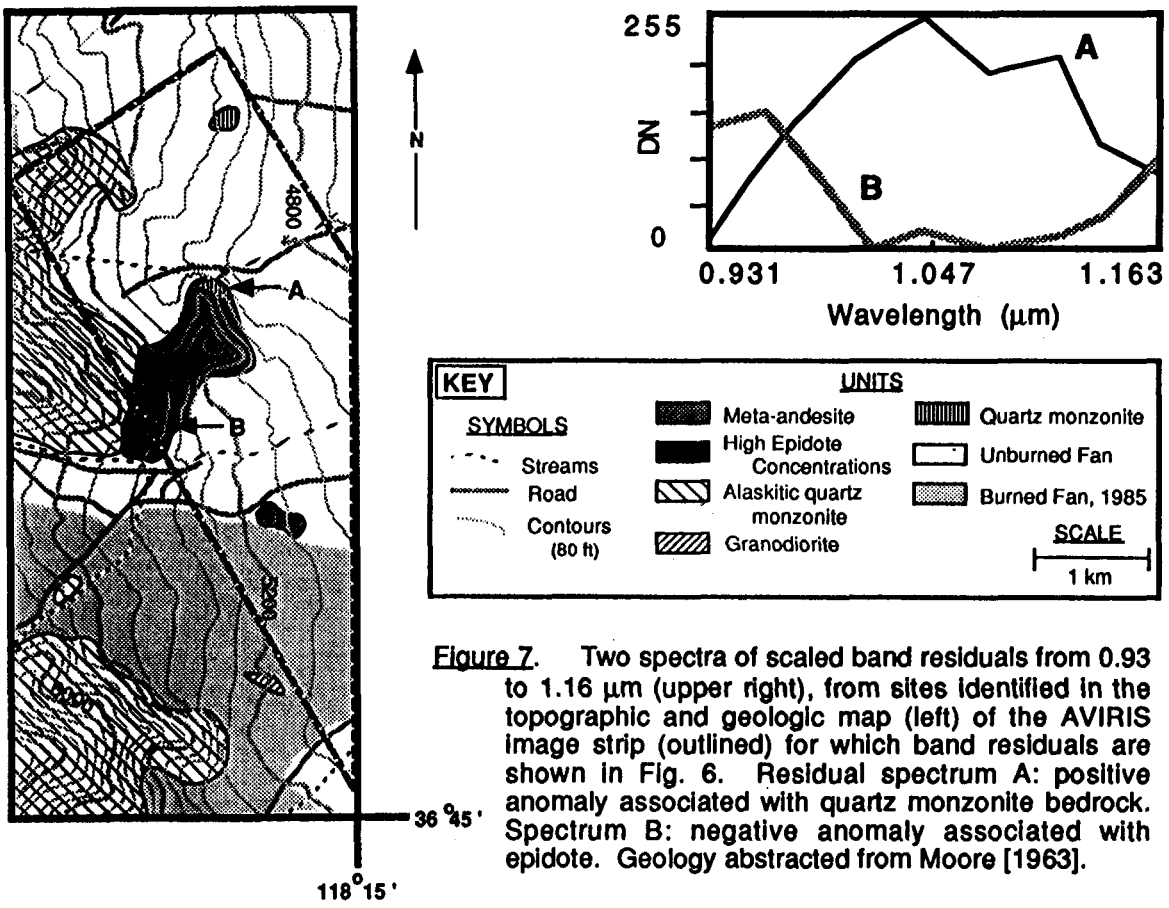

Figure 7. Two spectra of scaled band residuals from 0.93 to 1.16 μm (upper right), from sites identified in the topographic and geologic map (left) of the AVIRIS image strip (outlined) for which band residuals are shown in Fig. 6. Residual spectrum A: positive anomaly associated with quartz monzonite bedrock. Spectrum B: negative anomaly associated with epidote. Geology abstracted from Moore [1963].

spectrum B, from the south end of the ridge, is from one of the epidote-rich areas. Spectrum B shows a broad negative anomaly.

Pine Creek

The Pine Creek [Fox *et al.*, 1990] and Independence Creek areas are similar geologically. In both, lithologies are dominated by the granitic rocks of the Sierra Nevada, but metasedimentary rocks - especially marble - crop out near Pine Creek instead of the meta-andesite. As seen in Fig. 1, the AVIRIS image of Pine Creek was centered over the bajada, which here is dominated by a large moraine complex left by the Pleistocene glaciers of Pine Creek. Downstream from the terminus of the moraines are largely young gravelly sediments, covered locally by grassy meadows with denser stands of trees along distributaries of the creek. Especially south of the moraines, older deposits of bouldery debris flows are preserved.

The glaciations have controlled the alluviation history of the Pine Creek fan. Of chief interest in this study is the preservation of fan units of a broad range of ages and degrees of soil development. Fox et al. [1990] have characterized the volumetric clay concentrations in each unit of the chronosequence, and we seek to find associated anomalies near 2.2-μm in the residual spectrum. These are anticipated if no endmember accounts for clay alone, or if the depths of the clay OH^- bands are not proportional to the fraction of the clay-rich endmember.

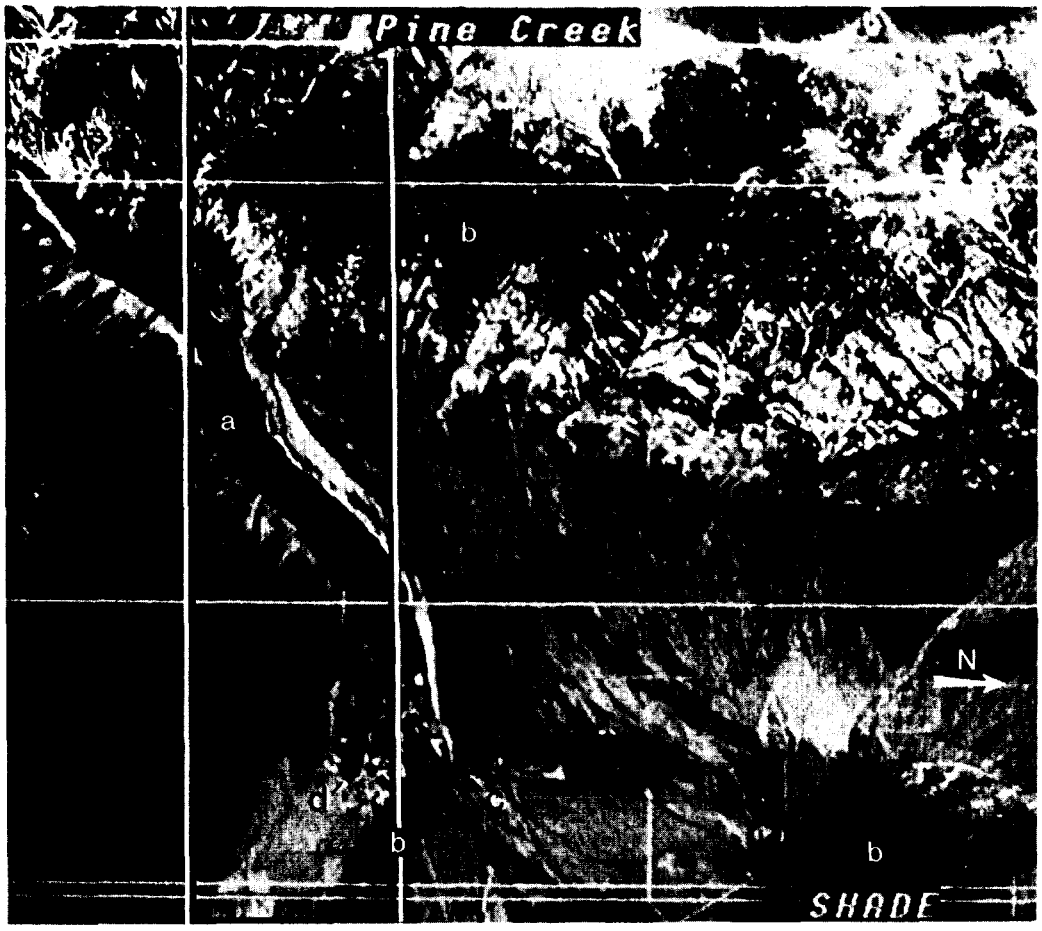

Figure 8. Shade fraction image, Pine Creek. Image has been inverted (complemented) such that high shade fractions are dark instead of light. Scene is ~8.5 km across. Rectangle shows the area for which band residuals were calculated. Letters *a* - *d* denote areas discussed in text.

The mixture model that was used was the same as for Independence Creek. However, alfalfa was used instead of *Coleogyne* for the vegetation endmember. The shade endmember fraction image is shown in Fig. 8, inverted to resemble a radiance image. The highest shade fractions (dark) are associated with north slopes (a) and dense stands of vegetation (b), especially below the terminus of the moraines (c, d).

Figure 9 shows seven residual images for the 2.2-μm window of Fig. 6c. The data were taken from the area outlined in Fig. 8. At Independence Creek, the continuum model accounted for all the spectral variance. At Pine Creek, more information is evident. The strongest anomaly is positive (light), associated with riparian vegetation along the stream (a). The positive residual is not directly correlated with a high fraction of shade. In the meadow area, both light and dark patterns are seen in all the images of Fig. 9 (b,c). Much of the alluvial fan south of Pine Creek (d) is dark in Fig. 9, again for all seven bands. This large region of negative anomaly contrasts with the mountain area (e), which has a neutral residual and was well modeled.

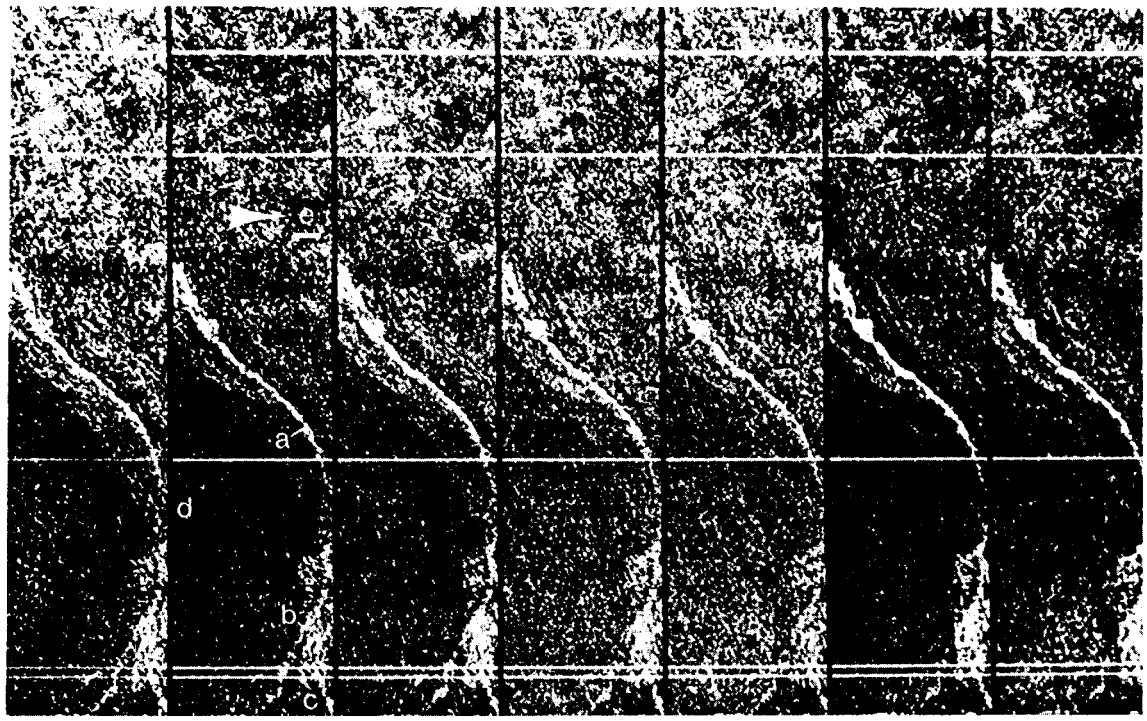

Figure 9. Strongly stretched band-residual images of Pine Creek, 2.19 - 2.25 μm. Letters *a* - *e* denote areas mentioned in text.

DISCUSSION

Although absorption features are always reflectance minima, anomalies in the residual spectrum can be higher or lower than the model continuum spectra. Negative residuals occur where there are absorption bands in the data not modeled by the endmembers. Positive residuals occur where the endmember spectra contain absorption features stronger than found in the data.

Areas of high rms residual either are deviant from the continuum model over much of the spectrum, or they must exhibit extremely strong deviations in a few bands. The correct explanation may be found by inspecting the band-residual images: global deviance will be expressed as light or dark anomalies over many or most of the band residuals, whereas local absorption features will appear in only a few bands. However, subtle local deviations of a few percent will not appear in the rms residual, even though they may be detected in the appropriate band residuals. It is these subtle local effects that we anticipate in the band-residual images for scenes such as Owens Valley.

The residual images we calculated resembled the radiance images: the light devegetated areas of the fire scars were associated with positive anomalies; the dark meta-andesite is associated with a negative residual; sunlit slopes are positive, and so forth. However, the residuals are not simply proportional to reflectance or radiance. For example, the correspondence of the residuals to the radiance data is not evident at

all wavelengths. Figures 6 and 9 show only three spectral windows for which there were strong residuals. Across the rest of the spectrum, they were much weaker. Even within the windows, close inspection shows that the supposed correspondence varies from unit to unit in the scene: the positive anomalies on the southeast perimeter of the fire scars appear in all three windows, whereas the stronger anomalies associated with the scars themselves are not evident in the ~2.2.-μm residuals. Anomalies associated with trees along Independence Creek have different signs in the different windows: they are positive in the visible and 1-μm regions, but negative at 2.2 μm. Yet in the radiance images, vegetation is relatively dark in the visible and light at 1 μm. Finally, the centers and widths of the anomalies differ for the various units: the positive anomaly near 0.6 μm for the old alluvial fan west of the 1947 fire scar on Symmes Creek is greater at 0.643 μm than for the young fan to the north, yet they are the same at 0.613 μm, and the sense is reversed at lower wavelengths. The conclusion is inescapable that the correspondence between residual and radiance is spurious.

Figure 7 shows that near 1 μm the anomalies over the meta-andesite and quartz monzonite at Independence Creek are equal in magnitude and bandwidth, yet opposite in sign. The meta-andesite has a negative anomaly because there was no endmember with strong Fe^{++} absorption, but why are the burn scars and quartz monzonite positive? A plausible explanation is that the endmember that spectrally most resembles granitic bedrock and soil exposed by the fire was sandy soil, which was actually sampled from an adjacent drainage containing more numerous mafic rocks, and hence more Fe^{++}. On the fire scars the top few cm of soil were removed by wind, and the granitic bedrock shed grus. Both processes expose unweathered soil or rock, and decrease the dilution of the granitic spectrum by vegetation, lichen, and weathering products. As a result, the spectrum is dominated by the Fe^{++}-poor quartz monzonite, with less absorption than the endmember. Hence, the residual spectrum is positive in the Fe^{++} absorption region.

According to this interpretation, the similar magnitudes of the anomalies are coincidental, but the similar bandwidths and centers are unexplained. The anomalies for the same sites, but at ~0.6 μm, are at different band centers and have different bandwidths, showing that the anomalies are not linked at all wavelengths. The differential effects observed for different soils may arise because the weathered horizons of the soils extend to different depths, but the æolian stripping is constant across different units.

Anomalies over sunlit (positive) and shaded (negative) slopes of the same material pose an interpretive challenge. In part, the pattern may be explained by a small error in the shade vector, such that the larger rms residual results simply from the high radiance. However, the burned fans also have a moderately high rms residual (~2 DN): twice that of the adjacent unburned fans. Because these fans are not a factor of two darker than the sunlit granite (Fig. 3), the residual must also represent a real difference between the spectra of the granite bedrock in the burned area and the reference sandy alluvium, as discussed above.

Some residuals appear to be related to patterns in vegetation abundance or type. The unburned fans near Boron Springs Creek had detectable negative residuals at red, but not green, wavelengths. This is explainable by increased leaf area, compared to the *Coleogyne* endmember; however supporting field observations have not been made. The anomaly along Independence Creek, especially near 1 μm, could be related to the concentration of trees there, yet the bandwidth is too narrow to correspond to the near-infrared plateau of vegetation. The positive anomaly along the fire-scar perimeter appears to be similar, but may be stronger: it is evident at 2.2 μm as well. Field observations suggest that this anomaly corresponds to a zone of dead shrubs, killed by the 1985 fire. There are no leaves, and the wood is much more reflective than the dark stems and bark of the *Coleogyne*. Hence, high positive anomalies are

likely over the reflective plateaus of the wood spectrum. We have not inspected the entire residual spectrum to establish this correlation.

Dry grass and brush were not modeled as endmembers, but where they occurred - at the distal ends of the fans - they were expressed as high fractions of the old, reddish soil endmember. Although the spectra are similar [Roberts *et al.*, 1990] they are not identical, and high residuals are expected, especially near the sharp OH^- bands near 2.2 μm. However, this area was outside of the residual image strips we computed.

At Pine Creek, alfalfa instead of *Coleogyne* was used as an endmember. Despite this, trees and meadows along the creek have positive residuals near 2.2 μm. The endmember was defined from irrigated fields; a suggested explanation is that the natural vegetation is water-stressed at this time of year, and less absorptive at 2.2 μm.

Spectral Discrimination and the Number of Endmembers

We anticipated that many more endmembers would be required for AVIRIS than for Landsat TM, but such was not the case. Why are there no more than four or five required for AVIRIS with 171 bands, when four are needed for TM with six? Generally, when less discrimination is achieved than expected, the problem is attributed to low sensitivity, or to a low signal/noise ratio (SNR). Without a high SNR, only strong spectral differences would be apparent, and few endmembers could be

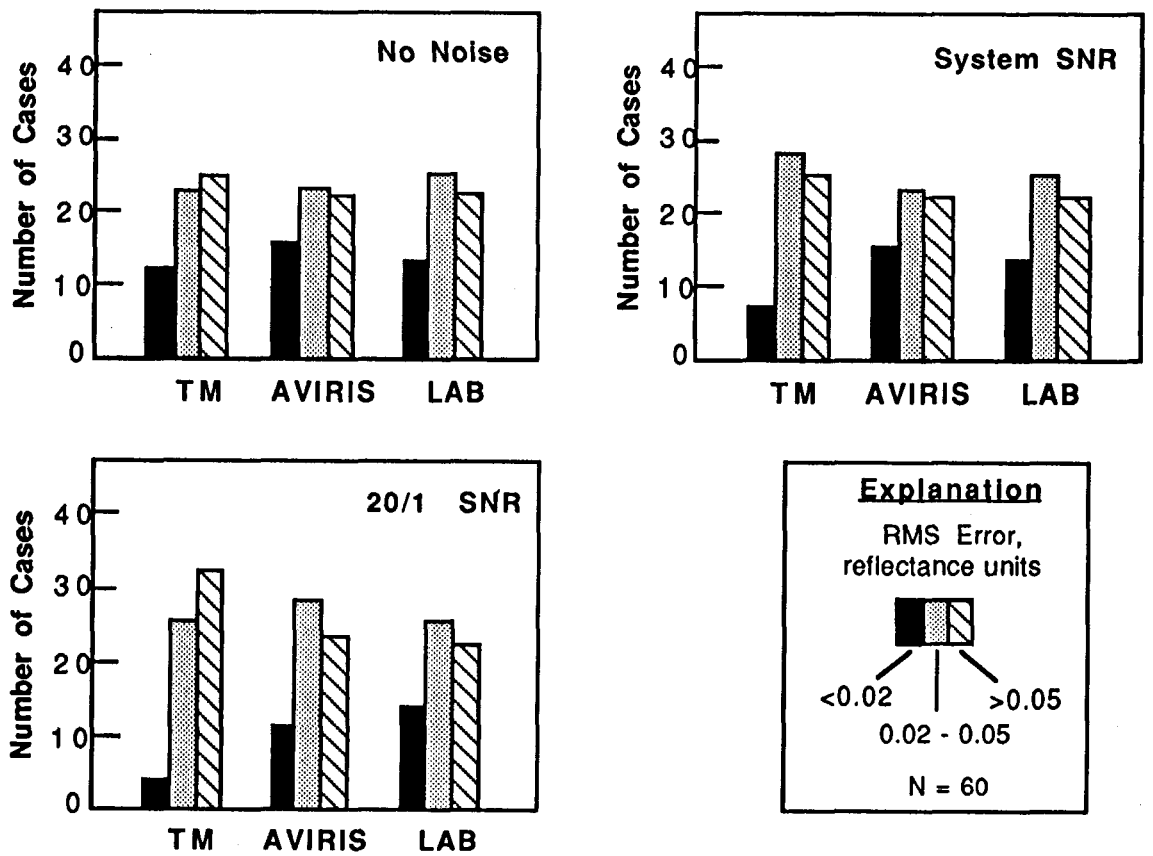

Figure 10. Spectrometer discrimination among 60 reference spectra. Well-modeled spectra have residuals of <0.02 reflectance units.

resolved. But important aspects of the continuum spectrum could be resolved using many measurements, even with lower SNR. Thus, the number of bands is a factor in discremination also. Low noise is required primarily to resolve narrow absorption features—that is, for the residual spectrum, not the continuum.

We explored the interplay of SNR and band number in spectral discrimination experimentally. One measure of spectral resolution or discrimination is the number of spectra that cannot be differentiated under a given set of sensor characteristics. We took the four endmember spectra used for the Independence Creek image and attempted to express 60 other reflectance spectra from the reference library as mixtures of these four. The finer the discrimination, the fewer spectra should be expressed well as mixtures. The particular spectra used did not matter, because the test was comparative. In this experiment, we simulated different SNR levels by adding random noise to the reflectance spectra. We sampled the spectra using three different sets of bands: the six bands of TM, the 171 of AVIRIS used in this study, and the 512 of our laboratory data (which covered the 1.4- and 1.9-μm windows excluded from the AVIRIS bands). We considered three cases: SNR = 0, SNR = 20, and SNR set to the instrument specifications: variable for AVIRIS, from 20 to 100; 90 for TM; and = 100 for the laboratory spectra. The first two cases bracketed the actual case. The spectra were modeled using equation 3, and the degree of fit was assessed using the rms-residual term. A fit was defined as "good" if the residual was < 0.02 reflectance units.

The results are tabulated in Figure 10, for three ranges of the rms residual. For the noiseless case and AVIRIS bands, 15 reference spectra were fit by mixtures of the four reference spectra with an rms residual of <2%, whereas for TM and the laboratory spectra, 12 and 13 spectra respectively were modeled at that level. For the second, pessimistic case (SNR = 20), the number of well-fit laboratory spectra was unchanged, whereas the number for AVIRIS was reduced by four and the number for TM was reduced by eight. For laboratory spectra, the number in the intermediate and poorly fit categories was unchanged; for AVIRIS, the number in the intermediate category increased; and for TM, the number of poorly fit spectra increased.

For the realistic case ("system SNR"), the number of spectra in all three categories was unchanged, for both laboratory and AVIRIS data. For TM, the number of well-fit spectra was reduced by seven, and the number in the intermediate category was increased by the same amount; the number of poorly fit spectra was unchanged.

Clearly, addition of noise to the spectra reduced discrimination most for the systems with the fewest bands. The SNR of AVIRIS does not seem to be the factor limiting discriminability, at least for continuum spectra, and AVIRIS data were nominally equal to laboratory data in this test. It follows that noise in AVIRIS data serves primarily to reduce the detectability of discrete absorption features, where the degradation of signal cannot be overcome by multiple measurements in nearby bands.

CONCLUSIONS

We found that, for desert surfaces of Owens Valley, the background spectra measured by AVIRIS could be described as linear mixtures of weakly and moderately weathered soils, vegetation, and shade. A fifth endmember, representing a second type of vegetation, would have been locally useful on the valley floor. The clay OH^- band in the weathered soil endmember spectrum near 2.2 μm, 0.03 reflectance units deep, was evidently sufficient to describe all the clay absorption in the scene, at the AVIRIS spectrometer D sensitivity and SNR levels. We did not detect the strong OH^- epidote bands near 2.3 μm, from which we infer that the area covered by epidote was nowhere more than ~15%.

At shorter wavelengths, AVIRIS is more sensitive, and shallower bands are thus detectable. We were able to see Fe^{++} features at 1 μm, for which the residual band depth was 0.03, too great to be explained by epidote alone. It seems likely that other ferrous minerals in the meta-andesite host rock must have contributed to this measured band depth.

Evidently, the continuum may be described by a small number of spectral endmembers and their fractions. This is a signal advantage of endmember analysis. The continuum spectra, containing most of the information in the 171 bands of AVIRIS data, may be described by four or five fraction images. This number appears to be inherent to the scene: doubling the number of bands does not increase it, and the dimensionality of TM, with only six bands, is roughly the same as of AVIRIS.

Endmember-fraction images have the advantage that they are thematically meaningful; that is, they depict proportions of spectrally distinct scene constituents as defined by the field scientist, not just radiant fluxes in a particular spectral band. The endmember fractions may be empirically quantifiable as proportions of scene constituents [e.g., Smith et al., 1990b]. Not only is there strong data compression, but the remaining data are rendered more digestible by the image interpreter.

Although hyperspectral data do not appear to be necessary to determine the continuum endmembers, they do define the model spectra with great precision, enabling fine distinctions to be made using the residual spectra. The removal of the continuum or background spectrum is a necessary precursor to analysis, or even recognition, of the absorption features in the residual spectrum. For example, near 2.2-μm woody plant material has a reflectance peak, at the same wavelengths at which OH^- in clays absorbs [e.g., Roberts et al., 1990]. By estimating the fraction of wood based on a large number of bands, the residual spectrum may be corrected for wood near 2.2 μm, resulting in a more accurate representation of the depth of the clay feature. Without characterization of the background, detection and identification of absorption bands may be uncertain.

Spectral mixture analysis is a means of calibrating AVIRIS data for instrumental, atmospheric and geometric effects such as sun elevation. This approach does not depend on simultaneous field spectra or preflight AVIRIS measurements, even though such data are useful [e.g., Smith et al., 1988a]. Another result of mixture analysis is the partitioning of scene radiance into "tangible" and ephemeral sources: namely, physical scene constituents and photometric shading and shadowing, respectively. The shade fraction image is dominated by topographic information. It has not yet been possible to separate low radiance due to "shade" from low radiance due to dark surfaces using only VNIR data; nevertheless, removal of shade has led to more time-invariant fractions for the tangible endmembers [Adams et al., 1990a].

We find linear spectral mixture analysis to be an effective tool in the analysis and interpretation of AVIRIS data. It is a productive strategy to consider spectra measured by AVIRIS as consisting of a continuum, which describes the general background shape, and a residual, which contains spectral contributions from unusual scene constituents and nonlinear effects, especially concentrated in narrow absorption bands.

Research reported herein was supported in part by the Land Processes Branch of the National Aeronautics and Space Administration.

REFERENCES

Adams, J. B., and Adams, J. 1984. Geologic mapping using Landsat MSS and TM images: Removing vegetation by modeling spectral mixtures. Third Thematic Conf. Remote Sens. for Expl. Geol., ERIM 2:615-622.

Adams, J. B., Kapos, V., Smith, M. O., Filho, R. A., Gillespie, A. R., and Roberts, D. A. 1990a. A new Landsat view of land use in Amazonia. Intl. Symp. on Primary Data Acquisition '90, ISPRS, submitted, Manaus, Brazil (June).

Adams, J. B., and McCord, T. B. 1972. Spectral reflectivity: Optical properties of mineral separates, glass and anorthositic fragments from Apollo Mare samples. Proc. Apollo 12 Lunar Sci. Conf. 3, 2183-219. MIT Press.

Adams, J. B., Smith, M. O., and Gillespie, A. R. 1989. Simple models for complex natural surfaces: A strategy for the hyperspectral era of remote sensing. Proc. IEEE Intl. Geosci. and Remote Sens. Symp. '89 I:16-21.

Adams, J. B., Smith, M. O., and Gillespie, A. R. 1990b. Imaging spectroscopy: Data analysis and interpretation based on spectral mixture analysis. *In* Pieters, C. M., and Englert, P. J., *eds.*, Remote Geochemical Analysis: Elemental and Mineralogical Composition, Lunar and Planetary Institute, Houston, TX, *in press.*

Adams, J. B., Smith, M. O., and Johnson, P. E. 1986. Spectral mixture modeling: A new analysis of rock and soil types at the Viking Lander 1 site. J. Geophys. Res. 91:8098-8122.

Aristotle, ca. 335 BC. Metaphysics, Book Alpha 3-4. R. Hope, *translator.* U. Michigan Press, Ann Arbor, 394 p.

Bierman, P. R., and Gillespie, A. R. 1990. Range fires: A significant factor in the dating and evolution of geomorphic surfaces. Geology, submitted.

Boardman, J. W. 1989. Inversion of imaging spectrometry data using singular value decomposition. Proc. IEEE Intl. Geosci. and Remote Sens. Symp. '89 pp. 2069-2072.

Buja, A., and Asimov, D. 1985. Grand Tour methods, an outline. Proc. 17th Symp. on the Interface, Computing Science and Statistics.

Burke, R.M., Lunstrom, S., Harden, J., Gillespie, A.R., and Berry, M. 1986. Soil chronosequence on eastern Sierra Nevada fans, CA, supports remote sensing studies. Geol. Soc. Am. Abstr. with Program 18(6):553.

Chittmeni, C. B. 1981. Estimation of proportions in mixed pixels through their region characterization. Proc. Machine Processing of Remote Sens. Data Symp., Purdue Univ., West Lafayette, IN, p. 292-303.

Chrien, T. G., Green, R. O., and Eastwood, M. 1990. Laboratory spectral and radiometric calibration of AVIRIS. Proc. Airborne Sci. Workshop: AVIRIS, Jet Propulsion Laboratory, Pasadena, CA., 4-5 June. *This volume.*

Clark, R. N., Middlebrook, B., Livo, E., and Gallagher, A. 1990. Material absorption band depth mapping of imaging spectrometer data using a complete band shape least-squares fit with library reference spectra. Proc. Airborne Sci. Workshop: AVIRIS, Jet Propulsion Laboratory, Pasadena, CA., 4-5 June. *This volume.*

Conel, J. E., and Alley, R. A. 1984. Lisbon Valley, Utah, uranium test site report. *In* The Joint NASA/Geosat Test Case Project Final Report, Part 2, Vol. 1, Sec 8 (Paley, H. N., *ed.*), AAPG Bookstore, Tulsa, OK, pp. 1-101.

Conel, J. E., Breugge, C., Carrere, V., Green, R. O., and Hoover, G. 1990. Validation of in-flight recovery of atmospheric water vapor. Proc. Airborne Sci. Workshop: AVIRIS, Jet Propulsion Laboratory, Pasadena, CA., 4-5 June. *This volume.*

Crist, E. P., and Cicone, R. C. 1984. A physically-based transformation of Thematic Mapper data - the TM tasseled cap. IEEE Trans. Geosci. Remote Sens. (3) GE-22:256-263.

Detechmendy, D. M., and Pace, W. H. 1972. A model for spectral signature variability for mixtures. Remote Sens. Earth Resources, Vol. I., F. Shahrokhi, ed., Tullahoma, TN, p. 596-620.

Diner, D. J., and Martonchik, J. V. 1984. Atmospheric transfer of radiation above an inhomogeneous non-Lambertian reflective ground - I. Theory. J. Quant. Spectros. Rad. Transf. 31:97-125.

Dozier, J. 1981. A method of satellite identification of surface temperature fields of subpixel resolution. Remote Sens. Environ. 11:221-229.

Fox, L. III, Fischer, A. F. III, Gillespie, A. R., and Smith, M. O. 1990. Investigation of AVIRIS imagery for application in differentiating soil chronosequences. Proc. Airborne Sci. Workshop: AVIRIS, Jet Propulsion Laboratory, Pasadena, CA., 4-5 June. *This volume.*

Gao, B-C, and Goetz, A. F. H. 1990. Column atmospheric water vapor retrieval from airborne spectrometer data. J. Geophys. Res, *in press.*

Gillespie, A. R., Abbott, E. A., and Hoover, G. 1986. Spectral basis for relative dating of granitic alluvial fans, Owens Valley, CA (abs.). Geol. Soc. Am. Abstr. with Program 18:614.

Gillespie, A. R., Smith, M. O., Adams, J. B., and Willis, S. C. 1990. Spectral mixture analysis of multispectral thermal infrared images. Proc. Airborne Sci. Workshop: TIMS, JPL Publication 90-55, Jet Propulsion Laboratory, Pasadena, CA., 6 June 1990.

Goetz, A. F. H., and Boardman, J. W. 1989. Quantitative determination of imaging spectrometer specifications based on spectral mixing models. Proc. IEEE Intl. Geosci. and Remote Sens. Symp. '89 pp. 1036-1039.

Goetz, A. F. H., Rowan, L. C., and Kingston, M. J. 1982. Mineral identification from orbit: Initial results from the shuttle multispectral infrared radiometer. Science 218, 1020-1024.

Goetz, A. F. H., Vane, G., Solomon, J. E., and Rock, B. N. 1985. Imaging spectrometry for earth remote sensing. Science 228:1147-1153.

Green, R. O., Carrere, V., and Conel, J. E. 1989. Measurement of atmospheric water vapor using the Airborne Visible/Infrared Imaging Spectrometer. Proc. 12th Workshop on Image Processing, Am. Soc. Photogramm. Remote Sens., *in press.*

Green, R. O., Conel., J. E., Bruegge, C., Carrere, V., Margolis, J., and Hoover, G. 1990. Laboratory spectral and radiometric calibration of AVIRIS. Proc. Airborne Sci. Workshop: AVIRIS, Jet Propulsion Laboratory, Pasadena, CA., 4-5 June. *This volume.*

Hallum, C. R. 1972. On a model for optimal proportions estimation for category mixtures. Proc. Eighth Int'l Symp. Remote Sens. Environ., Ann Arbor, MI, p. 951-958.

Hapke, B. 1981. Bidirectional reflectance spectroscopy. 1. Theory. J. Geophys. Res. 89:6329-6340.

Heimes, R. C. 1977. Effects of scene proportions on spectral reflectance in lodgepole pine. Unpublished Master's thesis, Colorado State Univ., Fort Collins, CO.

Horwitz, H. M., Lewis, J. T., and Pentland, A. P. 1975. Estimating proportions of objects from multispectral scanner data. Final Report, NSAS Contract NAS9-14123, NASA-CR-141862, 108 p.

Horwitz, H. M., Nalepka, R. F., Hyde, P. D., and Morgenstern, J. P. 1971. Estimating the proportions of objects within a single resolution element of a multispectral scanner. Proc. Seventh Int'l Symp. Remote Sens. Environ., Ann Arbor, MI, p. 1307-1320.

Huete, A. R. 1986. Separation of soil-plant spectral mixtures by factor analysis. Remote Sens. Environ. 19:237-251.

Huete, A. R., Jackson, R. D., and Post, D. F. 1985. Spectral response of a plant canopy with different soil backgrounds. Remote Sens. Environ. 17:37-53.

Jackson, R. D. 1983. Spectral indicies in n-space. Remote Sens. Environ. 13:409-421.

Johnson, P.E., Singer, R. B., Smith, M. O., and Adams, J. B. 1990. Quantitative determination of mineral abundances and particle sizes from reflectance spectra. J. Geophys. Res. in press.

Johnson, P.E., Smith, M. O., Taylor-George, S., and Adams, J. B. 1983. A semiempirical method for analysis of the reflectance spectra of binary mineral mixtures. J. Geophys. Res. 88:3557-3561.

Kauth, R. L., and Thomas, G. S. 1976. The tasseled cap - a graphic description of the spectral temporal development of agricultural crops as seen by Landsat. *Proc. 3rd Symp. Machine Processing of Remote Sens. Data*, LARS, Purdue, pp. 4B/41-4B/51

Marsh, S. E., Switzer, P., Kowalik, W., and Lyon, R. J. P. 1980. Resolving the percentage of component terrains within single resolution elements. Photogramm. Engr. and Remote Sens. 46:1079-1086.

Moore, J. G. 1963. Geology of the Mount Pinchot Quadrangle, southern Sierra Nevada, California. U. S. Geol. Survey Bull. 1130, 152 p.

Mustard, J. F., and Pieters, C. M. 1986. Quantitative abundance estimates from bidirectional reflectance measurements. J. Geophys. Res. pp. E617-E626.

Mustard, J. F., and Pieters, C. M. 1987. Abundance and distribution of ultramafic microbreccia in Moses Rock dike: Quantitative application of mapping spectroscopy. J. Geophys. Res. 92:10376-10390.

Nalepka, R. F., and Hyde, P. D. 1972. Classifying unresolved objects from simulated space data. Proc. Eighth Int'l Symp. on Remote Sens. of Environ., Ann Arbor, MI, p. 935-949.

Nash, D. B., and Conel, J. E. 1974. Spectral reflectance systematics for mixtures of powdered hypersthene, labradorite, and ilmenite. J. Geophys. Res. 79:1615-1621.

Otterman, J., Ungar, S., Kaufman, Y., Podolak, M. 1980. Atmospheric effects on radiometric imaging from satellites under low optical thickness conditions. Remote Sens Environ. 9:115-129.

Pace, W. H., and Detechmendy, D. M. 1973. A fast algorithm for the decomposition of multispectral data into mixtures. Remote Sens. Earth Resources, Vol. II., F. Shahrokhi, ed., Tullahoma, TN, p. 831-848.

Pech, R. P., Graetz, R. D., and Davis, A. W. 1986. Reflectance modelling and the derivation of vegetation indicies for an Australian semi-arid shrubland. Intl. J. Remote Sensing 7:389-403.

Pieters, C. M., Adams, J. B., Mouginis-Mark, P. J., Zisk, S. H., Smith, M. O., Head, J. W., and McCord, T. B. 1985. The nature of crater rays: The Copernicus example. J. Geophys. Res. 90:12392-12413.

Possolo, A., Adams, J., and Smith, M. 1990. Mixture models for multispectral images. J. Geophys. Res., submitted.

Ranson, K. J. 1975. Computer assisted classification of mixtures with simulated spectral signatures. Unpublished Master's thesis, Colorado State Univ., Fort Collins, CO.

Ranson, K. J., and Daugherty, C. S. T. 1987. Scene shadow effects on multispectral response. IEEE Trans. Geosci. and Remote Sens. GE-25(4):502-509.

Reid, M. J., Gancarz, A. J., and Albee, A. L., 1973. Constrained least-squares analysis of petrologic problems with an application to lunar sample 12040. Earth Planet. Sci. Lett. 17:433-445.

Richardson, A. J., Wiegand, C. L., Gausman, H. W., Cuellar, J. A., and Gerbermann, A. H., 1975. Plant, soil and shadow reflectance components of row crops. Photogramm. Engr. Remote Sens. 41:1401-1407.

Roberts, D. A., Adams, J. B., and Smith, M. O. 1990. Distribution of visible and near-infrared radiant flux above and below a transmittant leaf. Remote Sens. Environ., *accepted.*

Roberts, D. A., Smith, M. O., Adams, J. B., Sabol, D. E., Gillespie, A. R., and Willis, S. C. 1990. Isolating woody plant material and senescent vegetation from green vegetation in AVIRIS data. Proc. Airborne Sci. Workshop: AVIRIS, Jet Propulsion Laboratory, Pasadena, CA., 4-5 June. *This volume.*

Sabol, D. E., Adams, J. B., and Smith, M. O. 1990. Predicting the spectral detectability of surface materials using spectral mixture analysis. Proc. Int. Geosci. Remote Sens. Symposium '90 (IGARRS '90), 2:967-970.

Sacco, W. J., 1972. On mixture distributions in pattern recognition. Information Sciences 4:101:120.

Sasaki, K., Kawata, S., and Minami, S. 1983. Constrained nonlinear method for estimating component spectra from multicomponent mixtures. Appl. Optics 22:3599-3603.

Shipman, H., and Adams, J. B. 1987. Detectability of minerals on desert alluvial fans using reflectance spectra. J. Geophys. Res. 92:10391-10402.

Shippert, P., Bradshaw, G., and Willis, S. C. 1988. Washington Image and Spectral Package (WISP): Preliminary Documentation. Remote Sensing Laboratory, AJ-20., Dept. of Geological Sciences, University of Washington, Seattle, WA 98195, 194 pp.

Singer, R., and McCord, T. B. 1979. Mars: Large scale mixing of bright and dark surface materials and implications for analysis of spectral reflectance. Proc. 10th Lunar Planet. Sci. Conf. p. 1835-148.

Smith, M. O., and Adams, J. B. 1985a. Strategy for analyzing mixed pixels in remotely sensed imagery. Proc. NASA/JPL Aircraft SAR Workshop JPL Publ. 85-39, p. 47-48.

Smith, M. O., and Adams, J. B. 1985b. Interpretation of AIS images of Cuprite, Nevada, using constraints of spectral mixtures. Proc. Airborne Imaging Spectrometer Data Analysis Workshop JPL Publ. 85-41, p. 62-68.

Smith, M. O., Adams, J. B., and Gillespie, A. R. 1988a. Evaluation and calibration of AVIRIS test-flight data: Owens Valley, CA. Final Report NASA CONTRACT No. NAGW 1135, 17 p.

Smith, M. O., Adams, J. B., and Gillespie, A. R. 1990c. Reference endmembers for spectral mixture analysis. Proc. 5th Australasian Conf. on Remote Sens., Perth, Australia, 8-12 Oct.

Smith, M. O., Johnson, P. E., and Adams, J. B. 1985. Quantitative determination of mineral types and abundances from reflectance spectra using principal components analysis. Proc. 15th Lunar Planet. Sci. Conf. Part 2. J. Geophys. Res., 90, Suppl., pp. C797-C804.

Smith, M. O., Roberts, D. A., Shipman, H. M., Adams, J. B., Willis, S. C., and Gillespie, A. R. 1988b. Calibrating AIS images using the surface as reference. Proc. Airborne Imaging Spectrometer Workshop III (June), JPL Publ. 88-30, p 63-69, Jet Propulsion Laboratory, Pasadena, California.

Smith, M. O., Ustin, S. L., Adams, J. B., and Gillespie, A. R. 1990a. Vegetation in deserts: I. A regional measure of abundance from multispectral images. Remote Sens. Environ. 31:1-26.

Smith, M. O., Ustin, S. L., Adams, J. B., and Gillespie, A. R. 1990b. Vegetation in deserts: II. Environmental influences on regional abundance. Remote Sens. Environ. 31:27-52.

Suits, G. H. 1972. The cause of azimuthal variations in directional reflectance of vegetative canopies. Remote Sens. Environ. 22:175-182.

van den Bosch, J. M., and Alley, R. E. 1990. Application of LOWTRAN 7 as an atmospheric correction to AVIRIS data. Proc. Airborne Sci. Workshop: AVIRIS, Jet Propulsion Laboratory, Pasadena, CA., 4-5 June. *This volume.*

Vane, G., and Goetz, A. F. H. 1988. Terrestrial imaging spectroscopy. Remote Sens. Environ. 24, 1 -29.